JⱮ PAPERS

# Vortex ring breakdown dominating the entrainment of a synthetic jet

**Congyi Xu**[1] **and Jinjun Wang**[1],†

[1]Fluid Mechanics Key Laboratory of Education Ministry, Beihang University, Beijing 100191, PR China

The understanding of the entrainment mechanism of synthetic jets can help optimise the synthetic jet actuators in engineering applications. It is generally believed that vortex rings or strong velocity fluctuations in the near field of the synthetic jet are responsible for its enhanced entrainment. However, in recent years, it has been found that the enhanced entrainment of the synthetic jet may be caused by the instability or the vortex ring breakdown in the transition region. To shed new light on this issue, synthetic jets with different Reynolds numbers and dimensionless stroke lengths are investigated with time-resolved two-dimensional particle image velocimetry. Based on the analyses of velocity triple-decomposition, Fourier mode decomposition and phase-averaged $\lambda_{ci}D/U_0$ field, the streamwise positions of the vortex ring breakdown are determined for the synthetic jets, and the entrainment coefficient can be divided into three components, i.e. the coherent turbulent kinetic energy production, the random turbulent kinetic energy production and the shape of the velocity profile. It is found that the entrainment coefficient is dominated by the component related to the random turbulent kinetic energy production, and reaches its peak value at the position of vortex ring breakdown. The results obtained in different cases show a strong correlation between vortex ring breakdown and entrainment enhancement. From the perspective of instantaneous snapshot, the mechanism of vortex ring breakdown enhanced entrainment is revealed, that is, vortex ring breakdown enhanced the small-scale vortex near the turbulent/non-turbulent interface, resulting in an increase of enstrophy production, and thus enhanced local entrainment.

**Key words:** jets, turbulent mixing, mixing enhancement

## 1. Introduction

The synthetic jet (James, Jacobs & Glezer 1996; Smith & Glezer 1998) is a new type of active flow control technique developed over the past two decades. Due to their advantages of no external air source, simple actuator structure and enhanced entrainment

characteristics, synthetic jets have been applied in flow control fields such as fluid mixing (Zhang *et al.* 2021*a*), suppression of flow separation (Feng & Wang 2012; Zong, van Pelt & Kotsonis 2018) and enhancement of heat transfer (Krishan, Aw & Sharma 2019; Xu *et al.* 2019). Therefore, revealing the entrainment mechanism of synthetic jets can help to optimise the design and arrangement of synthetic jet actuators in engineering applications.

The behaviour of synthetic jets has been extensively studied through experimental and numerical methods, and the insights into the entrainment mechanism of synthetic jets have been proposed. Mallinson, Reizes & Hong (2001) studied the flow produced by a synthetic jet actuator with a circular orifice. It was found that the synthetic jet establishes self-similarity much more rapidly than the continuous jet, primarily because of turbulent dissipation. They suggested that the 'flow oscillations introduced by the synthetic jet' cause a greater entrainment in contrast to the case of the continuous jet. Cater & Soria (2002) conducted experimental studies on round synthetic jets and continuous jets. They found that the synthetic jet has a cross-stream velocity distribution similar to that of the continuous jet, but has a larger spreading rate and a more rapid centreline velocity decay. They believed that the 'large-scale structure' is responsible for a peak in the radial entrainment in the near field of the synthetic jet, and the difference of near-field flow structure between the two jets is the reason for the difference of streamwise velocity gradients, spreading rate and centreline velocity decay. Similar results were found in the experimental study of two-dimensional synthetic jets and continuous jets with the same Reynolds number by Smith & Swift (2003). The results indicated that the synthetic jet has a larger growth rate of volumetric flow in the near field, which is attributed to the fact that the 'rollup of the synthetic jet vortex pair' entrains much more fluid. Krishnan & Mohseni (2009) modelled the synthetic jet using both the Schlichting solution to boundary-layer equations in cylindrical polar coordinates and the Landau–Squire solution to the Navier–Stokes equations in polar coordinates, and found that the eddy viscosity of the synthetic jet is larger than an equivalent continuous jet. They attributed the enhanced eddy viscosity to the additional mixing caused by the initial introduction of the periodic vortex structures and their subsequent breakdown and transition to turbulence. In summary, these earlier studies attributed the enhanced entrainment of synthetic jets to the effect of vortex rings or strong velocity fluctuations.

With the development of experimental techniques and computational power, turbulent/non-turbulent interfaces (TNTIs) in jets (Westerweel *et al.* 2005, 2009; Mistry *et al.* 2016; Breda & Buxton 2019; Mistry, Philip & Dawson 2019), wakes (Kankanwadi & Buxton 2020, 2022; Chen & Buxton 2023), turbulent boundary layers (Chauhan *et al.* 2014; Borrell & Jimenez 2016; Long, Wang & Pan 2022; Zhang, Watanabe & Nagata 2023), mixing layers (Jahanbakhshi & Madnia 2016, 2018; Balamurugan *et al.* 2020) and other flows (Zhang, Rival & Wu 2021*b*; Li, Long & Wang 2022) have been studied to understand the turbulent entrainment process. The TNTI is a very thin fluid layer that separates turbulent and non-turbulent flows (da Silva *et al.* 2014). The TNTI contains a viscous superlayer dominated by viscous diffusion and a turbulent sublayer dominated by enstrophy production. The boundary between the viscous superlayer and the non-turbulent region is the irrotational boundary. From the perspective of an instantaneous snapshot, entrainment is the process by which irrotational fluid from the environment enters the turbulent region through the TNTI, visually divided into two parts: nibbling and engulfment (Jahanbakhshi & Madnia 2016; Mistry *et al.* 2016). Nibbling refers to the vorticity propagation process along the TNTI and is related to the small-scale structure near the TNTI. The small-scale structure near the TNTI influences the entrainment process by modifying the strain field near the TNTI (Mistry *et al.* 2019) and the production of the

TNTI area (Neamtu-Halic *et al.* 2020). Engulfment refers to the process where irrotational fluid from the environment is drawn into the turbulent region by the inviscid motion associated with large-scale structures. Despite the presence of large-scale vortex rings in the near field of the synthetic jet, it has been confirmed that the engulfment process is not the dominant entrainment process (Xu, Long & Wang 2023). The contribution of engulfment to the entrainment process in the synthetic jet does not exceed 4 %, consistent with previous studies on continuous jets (Mathew & Basu 2002; Westerweel *et al.* 2005, 2009; Taveira *et al.* 2013).

Therefore, it is necessary to reconsider what causes the enhanced entrainment in synthetic jets. In recent years, it has been observed that enhanced entrainment of synthetic jets occurs in the transition region between the near field dominated by vortex rings and the far field where the flow is fully developed (Xia & Mohseni 2018; Xu *et al.* 2023). Xia & Mohseni (2018) suggested that the enhanced spreading rate and the centreline velocity decay in the transition region are caused by the enhanced mode of mixing related to the forced instability of the pulsed large vortices. Xu *et al.* (2023) suggested that the 'breakdown of the vortex ring', instead of the vortex ring, enhances the entrainment in the synthetic jet based on the experimental data of a single case. However, to the best of our knowledge, studies on the origin of enhanced entrainment in the transition region of synthetic jets are still insufficient, and the mechanism remains unclear.

This paper aims to achieve quantitative determination of the position of vortex ring breakdown and the peak position of the entrainment coefficient while simultaneously establishing their correlation. Additionally, the mechanism of vortex ring breakdown leading to entrainment enhancement is revealed from the perspective of an instantaneous snapshot of the vortex evolution near the TNTI.

## 2. Experimental methods

### 2.1. *Apparatus*

A brief description of the synthetic jet actuator is provided here, and detailed information about the device can be found in previous work (Xu *et al.* 2023). In the present experiment, the synthetic jet is produced by an actuator based on a piezoelectric ceramic diaphragm. A sinusoidal signal is generated by the Tektronix AFG1062 signal generator, amplified by the Aigtek ATA-214 voltage amplifier and then applied to the piezoelectric ceramic diaphragm to generate a synthetic jet at the orifice with diameter $D = 5$ mm. The flow at the orifice of the synthetic jet actuator is measured by the HangHua CTA-02A hot-wire anemometer. The uncertainty of the hot-wire measurement is approximately 0.2 %. The hot-wire probe measures the flow velocity at the orifice at a sampling frequency of 40 kHz. A sinusoidal function is used to fit the velocity of the blowing period to obtain the maximum velocity $U_{max}$ during the excitation period. The frequency and voltage characteristics of the synthetic jet actuator are shown in figure 1. According to Smith & Swift (2003), the time-averaged blowing velocity $U_0$ at the synthetic jet actuator orifice can be calculated from

$$U_0 = \frac{1}{T} \int_0^{T/2} u_0(t) \, dt, \tag{2.1}$$

where the velocity $u_0(t)$ at the synthetic jet actuator orifice can be described by the sinusoidal function $u_0(t) = U_{max} \sin(2\pi f_d t)$; $T = 1/f_d$ is the excitation period. Reynolds number and dimensionless stroke length are two important parameters to characterise synthetic jets (Smith & Swift 2003; Shuster & Smith 2007). The jet Reynolds number $Re_j$ based on the time-averaged blowing velocity $U_0$ and the orifice diameter $D$ is
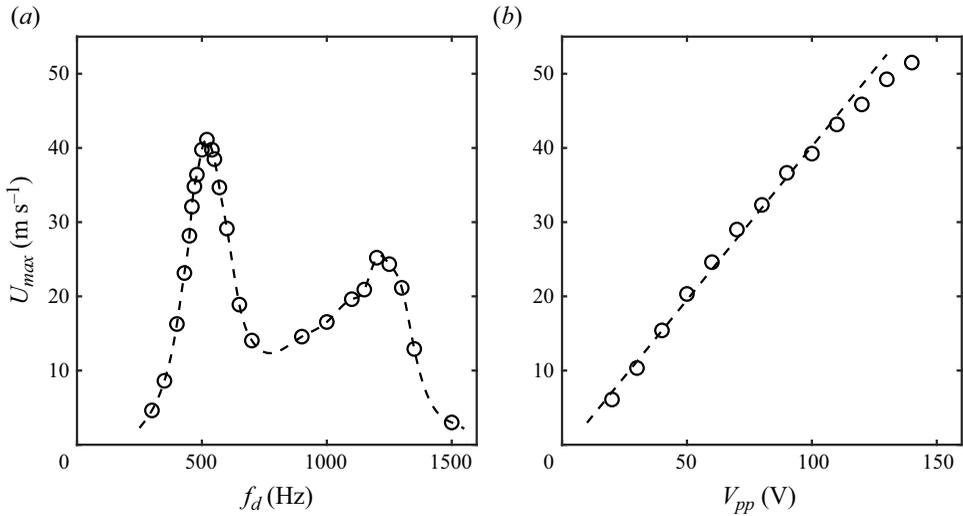
Figure 1. (*a*) Frequency characteristics of the synthetic jet actuator at $V_{pp} = 100$ V. (*b*) Voltage characteristics of the synthetic jet actuator at $f_d = 500$ Hz. Here $f_d$ and $V_{pp}$ are the driving frequency and driving voltage of the actuator, respectively.

defined as

$$Re_j = \frac{U_0 D}{\nu}, \tag{2.2}$$

where $\nu$ is the kinematic viscosity. The stroke length $L_0$ is normalised by the orifice diameter $D$ and the dimensionless stroke length can be denoted by

$$L_0/D = \frac{U_0 T}{D}. \tag{2.3}$$

In the present experiment, the driving frequency $f_d$ of the piezoelectric ceramic diaphragm is set at the resonance frequency of 500 Hz, and the time-averaged blowing velocity $U_0$ at the orifice is adjusted by changing the driving voltage $V_{pp}$. Therefore, both the jet Reynolds number $Re_j$ and the dimensionless stroke length $L_0/D$ are proportional to $U_0$. The jet Reynolds numbers for the three synthetic jets studied in the present experiment are 1050, 3150 and 4200, respectively. The corresponding dimensionless stroke lengths are 1.27, 3.82 and 5.09, respectively, which conform to the formation criteria $L_0/D > 0.5$ for axisymmetric synthetic jets (Holman *et al.* 2005). Hereafter, the three synthetic jets mentioned above will be referred to as Case 1, Case 2 and Case 3, respectively.

### 2.2. *Particle image velocimetry measurement*

Time-resolved two-dimensional particle image velocimetry (TR-2DPIV) experiments are conducted in a container of size $0.5\,\text{m} \times 0.5\,\text{m} \times 1\,\text{m}$. The coordinate system is defined in figure 2, and the centre of the orifice is taken as the origin. A laser sheet produced by the Beamtech Vlite-Hi-527 Nd:YAG dual-cavity laser illuminates the *x*–*y* plane through the jet centreline. The particle images are captured by the Photron Nova R2 high-speed camera with a Nikon 50 mm lens and processed by the multipass iterative Lucas–Kanade algorithm (Champagnat *et al.* 2011; Pan *et al.* 2015) to obtain the velocity field. For each jet, the experiments are conducted in three fields of view (FOV), as detailed in table 1. The uncertainty of particle displacement is approximately 0.1 pixels. The relative uncertainties
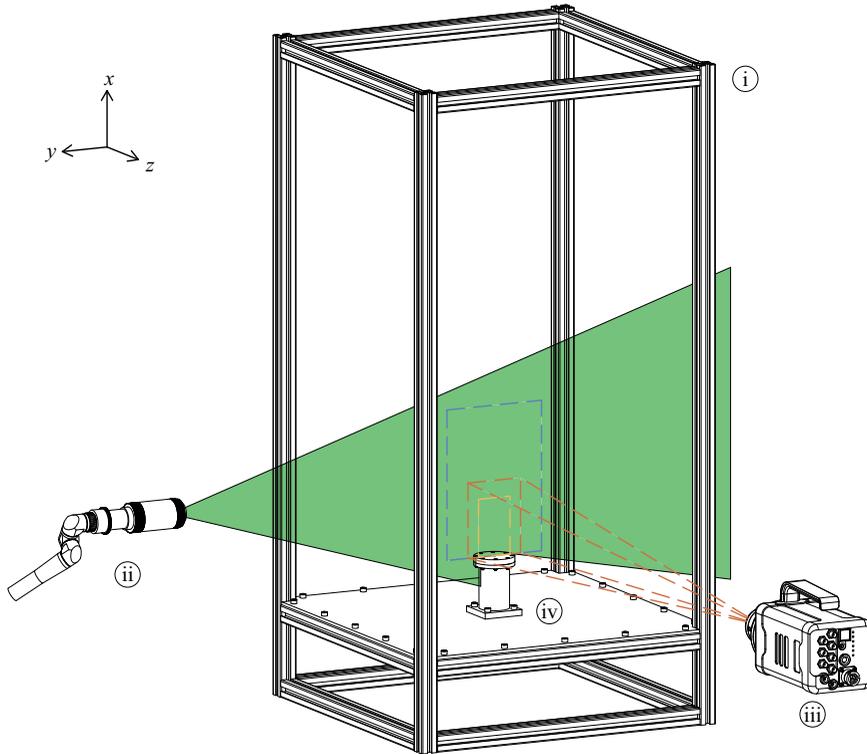
Figure 2. Schematic of the (i) container, (ii) laser head connected to a light arm, (iii) high-speed camera and (iv) synthetic jet actuator.

| Experiment details | FOV1 (yellow) | FOV2 (red) | FOV3 (blue) |
|---|---|---|---|
| Range of FOV | $0 \leq x/D \leq 20$ | $0 \leq x/D \leq 26$ | $0 \leq x/D \leq 52$ |
| Image size | $1024 \times 672$ | $1792 \times 1408$ | $2048 \times 1472$ |
| Interrogation window | $32 \times 32$ | $32 \times 32$ | $32 \times 32$ |
| Overlap | 75 % | 75 % | 75 % |
| Sampling frequency (Hz) | 3000 | 1000 | 500 |
| Number of realisations | 30 000 | 7500 | 7500 |

Table 1. Particle image velocimetry experiment details.

of flow velocity are no more than 1 % for the three FOV, calculated by the flow velocity uncertainty relative to the maximum velocity in the flow.

## 3. Results and discussion

### 3.1. *Velocity triple-decomposition*

The velocity $u$ in the flow field can usually be decomposed into a time-averaged velocity $\bar{u}$ and a fluctuation velocity $u'$. For periodic or quasiperiodic flows, the fluctuation velocity $u'$ can be further decomposed into a periodic fluctuation velocity $\tilde{u}$ and a random fluctuation velocity $\hat{u}$, i.e. velocity triple-decomposition (Reynolds & Hussain 1972; Feng &
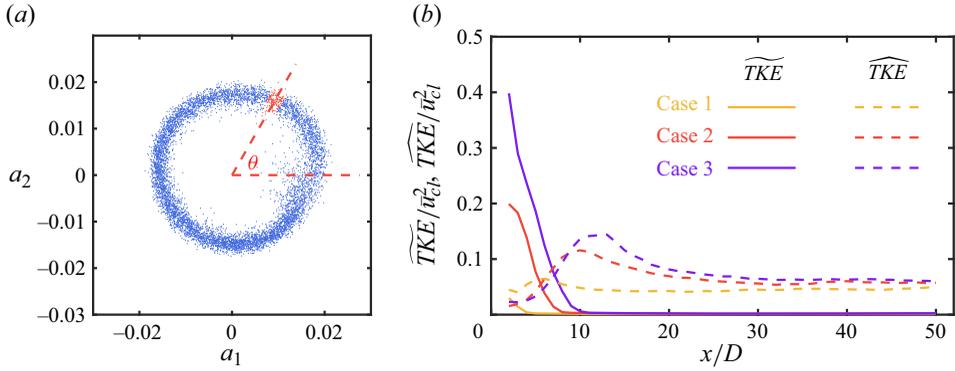
**980** A5-5

Figure 3. (*a*) Limit cycle formed by time coefficients $a_1$ and $a_2$ that correspond to the first and second modes of the POD, respectively. (*b*) Variations of the turbulent kinetic energy *TKE*, coherent turbulent kinetic energy $\widetilde{TKE}$ and random turbulent kinetic energy $\widehat{TKE}$, normalised by the local mean jet centreline velocity $\bar{u}_{cl}$.

Wang 2010)

$$u = \bar{u} + \tilde{u} + \hat{u}. \tag{3.1}$$

The periodic fluctuation velocity $\tilde{u}$ and the random fluctuation velocity $\hat{u}$ are, respectively, defined as

$$\tilde{u} = \langle u \rangle_{phase} - \bar{u}, \tag{3.2}$$

$$\hat{u} = u - \langle u \rangle_{phase}, \tag{3.3}$$

where $\langle \cdot \rangle_{phase}$ represents phase average. The periodic fluctuation velocity $\tilde{u}$ reflects the contribution of large-scale coherent structures, while the random fluctuation velocity $\hat{u}$ reflects the influence of small-scale turbulent structures.

The classical Reynolds stress can be obtained based on the total fluctuation velocity $u'$. Similarly, the coherent Reynolds stress and the random Reynolds stress can be obtained based on the periodic fluctuation velocity $\tilde{u}$ and the random fluctuation velocity $\hat{u}$, respectively. The three mentioned above have the following relationship (Feng & Wang 2010):

$$\overline{s'q'} = \overline{\tilde{s}\tilde{q}} + \overline{\hat{s}\hat{q}}, \tag{3.4}$$

where $s$ and $q$ represent arbitrary combinations of the velocity components $u$ and $v$. In addition, the turbulent kinetic energy *TKE* can be decomposed into coherent turbulent kinetic energy $\widetilde{TKE}$ and random turbulent kinetic energy $\widehat{TKE}$, and there is a relation

$$TKE = \widetilde{TKE} + \widehat{TKE} = \tfrac{1}{2}\overline{\tilde{u}_i\tilde{u}_i} + \tfrac{1}{2}\overline{\hat{u}_i\hat{u}_i}. \tag{3.5}$$

The phase information of the periodic or quasiperiodic flows can be extracted from the proper orthogonal decomposition (POD) time coefficient. Details of this method have been provided in previous work (Pan, Wang & Wang 2013; Xu *et al.* 2023). The phase angle $\theta$ of the snapshot can be obtained from the limit cycle formed by the time coefficients $a_1$ and $a_2$ corresponding to the first and second modes of the POD, respectively, as shown in figure 3(*a*). The mean value of the snapshots with $\theta \pm 5°$ is taken as the phase average, and the velocity triple-decomposition is applied to the flow field. It has been checked that the variation of the bin width for $\theta$ from $\theta \pm 1°$ to $\theta \pm 10°$ does not influence the conclusions in this paper. The coherent turbulent kinetic energy $\widetilde{TKE}$ and random turbulent

**980** A5-6

kinetic energy $\widehat{TKE}$ along the jet centreline are shown in figure 3(*b*). The coherent turbulent kinetic energy $\widehat{TKE}$ associated with the large-scale vortex ring dominates the region near the orifice, and gradually decreases to zero as the vortex ring breaks down downstream. In contrast, the random turbulent kinetic energy $\widetilde{TKE}$ gradually increases, reaches a peak value when the coherent turbulent kinetic energy $\widehat{TKE}$ is dissipated, and then gradually decreases to a constant value in the far field. This indicates the process of vortex ring breakdown and the transition of turbulent kinetic energy from large-scale to small-scale.

### 3.2. *Fourier mode decomposition*

To determine the dominant region of the vortex ring, Fourier mode decomposition (FMD) (Ma *et al.* 2015) is applied to the synthetic jet flow field. This method decomposes the flow field data containing multifrequency information into a series of modes according to the characteristic frequency, with each mode corresponding to a specific frequency coherent structure. The following is a brief introduction to FMD.

In the experiment, a time discrete signal $f_n = f(n\Delta t)$ at a certain point in space is obtained, where $0 \leq n \leq N$, $\Delta t = 1/f_s$. Here $N$ is the sampling number; $f_s$ is the sampling frequency. The discrete Fourier transform of the signal is as follows:

$$f_n = \sum_{k=0}^{N-1} c_k e^{i(2\pi k/N)n},\tag{3.6}$$

where

$$c_k = \frac{1}{N} \sum_{n=0}^{N-1} f_n e^{-i(2\pi k/N)n}.\tag{3.7}$$

A series of two-dimensional slice data for snapshots are arranged in the temporal dimension to form a three-dimensional matrix $\boldsymbol{F_n}$. Applying the Fourier transform to each grid point in space extends the single-point Fourier transform to the entire flow field, yielding a matrix

$$\boldsymbol{c_k} = \frac{1}{N} \sum_{n=0}^{N-1} \boldsymbol{F_n} e^{-i(2\pi k/N)n}\tag{3.8}$$

that contains the spectral information of the entire flow field. Matrix $\boldsymbol{c_k}$ can also be written as

$$\boldsymbol{c_k} = \tfrac{1}{2}\boldsymbol{A_k} e^{-i\varphi_k} = \tfrac{1}{2}\boldsymbol{A_k}(\cos\varphi_k - i\sin\varphi_k),\tag{3.9}$$

where $\boldsymbol{A_k} = 2|\boldsymbol{c_k}|$, $\varphi_k = -\arg \boldsymbol{c_k}$. $\boldsymbol{A_k}$ is referred to as the global amplitude spectrum, $\varphi_k$ is referred to as the global phase spectrum and $\boldsymbol{c_k}$ is referred to as the dynamic mode or the Fourier mode. The Frobenius norm of $\boldsymbol{A_k}$, namely $\|\boldsymbol{A_k}\| = \sqrt{\sum a_{ij}^2}$ ($a_{ij}$ is the element of the matrix $\boldsymbol{A_k}$), is defined as the global power spectrum.

The global power spectra based on the streamwise fluctuation velocity $u'$ are shown in figure 4. The global power spectra for the three cases have clear peaks at $f/f_d = 1$ and $f/f_d = 2$, corresponding to the driving frequency of the actuator and its harmonics. It indicates that the vortex ring generated by the actuator dominates the near field of the synthetic jet. The periodic evolution of the vortices is accompanied by the periodic variations of the velocities, and the FMD method can trace or map the vortex behaviours with the specified characteristic frequency (Ma *et al.* 2015). Figure 5 presents the
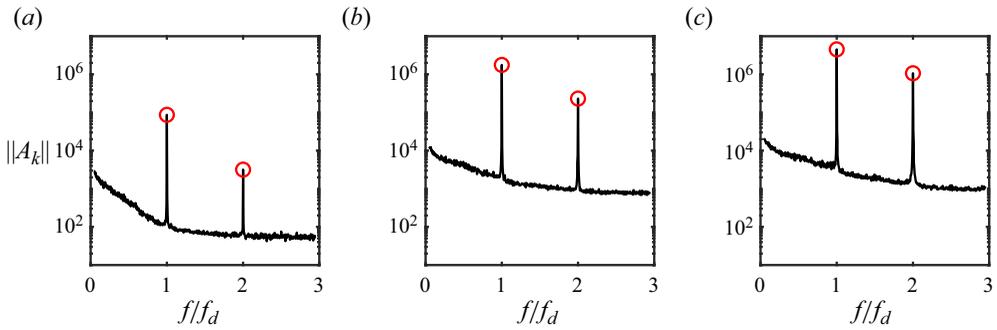
Figure 4. Global power spectra based on the streamwise fluctuation velocity $u'$ for (*a*) Case 1, (*b*) Case 2 and (*c*) Case 3. The red circle marks the peak position.
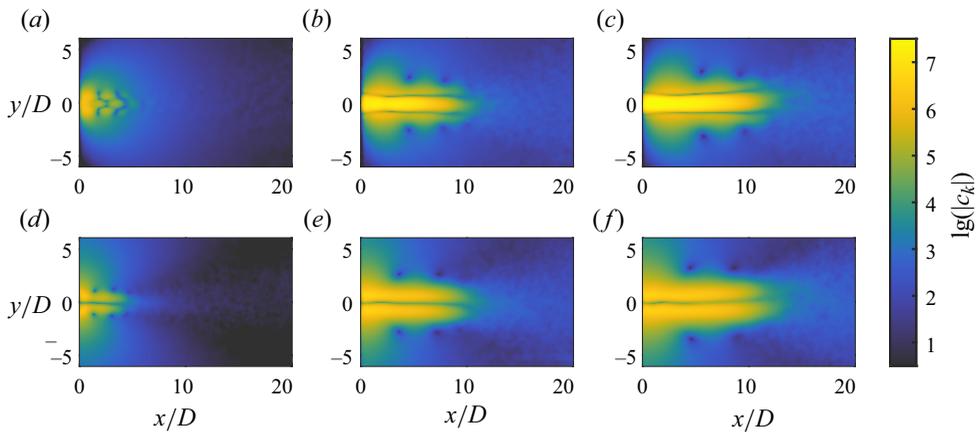


Figure 5. Amplitude of the Fourier mode for (*a,d*) Case 1, (*b,e*) Case 2 and (*c,f*) Case 3 at the characteristic frequency of $f/f_d = 1$, based on the (*a–c*) streamwise fluctuation velocity $u'$ and (*d–f*) the radial fluctuation velocity $v'$.

amplitude of the Fourier mode at the characteristic frequency of $f/f_d = 1$. The region with high-amplitude represents the region dominated by the vortex ring. The low-amplitude regions on both sides of the centreline in figure 5(*a–c*) can be considered as the trajectory of the vortex core, since the streamwise fluctuation velocity in this region is less affected by the vortex. The presence of some low-amplitude regions near the centreline of the near field in figure 5(*a*) may be due to the short stroke in this case, causing these locations to be affected by both the formed vortex ring and the suction cycle, producing a state similar to the node of the standing wave. Similarly, the low-amplitude region on the centreline in figure 5(*d–f*) can be considered as the centre of the vortex ring, and the radial fluctuation velocity in this region is less affected by the vortex. As the flow develops, the vortex rings break down, accompanied by the disappearance of the high-amplitude region. To determine the vortex ring breakdown position, the amplitudes of the Fourier mode based on the radial fluctuation velocity $v'$ at the characteristic frequency of $f/f_d = 1$ along the lines around the edge of the orifice (i.e. $y/D = 0.5$) are plotted in figure 6. The approximate linear decreasing parts of the curve are fitted linearly, and the position where the curve decline rate suddenly becomes smaller is taken as the position where the vortex
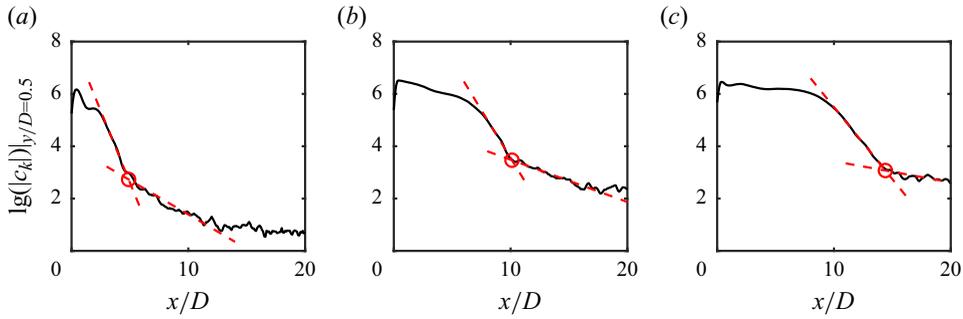
**980** A5-8

Figure 6. Amplitude of the Fourier mode for (*a*) Case 1, (*b*) Case 2 and (*c*) Case 3 at the characteristic frequency of $f/f_d = 1$ along the line $y/D = 0.5$, based on the radial fluctuation velocity $v'$. The red dashed lines and circles represent the fitting lines and the intersection points of the fitting lines, respectively.
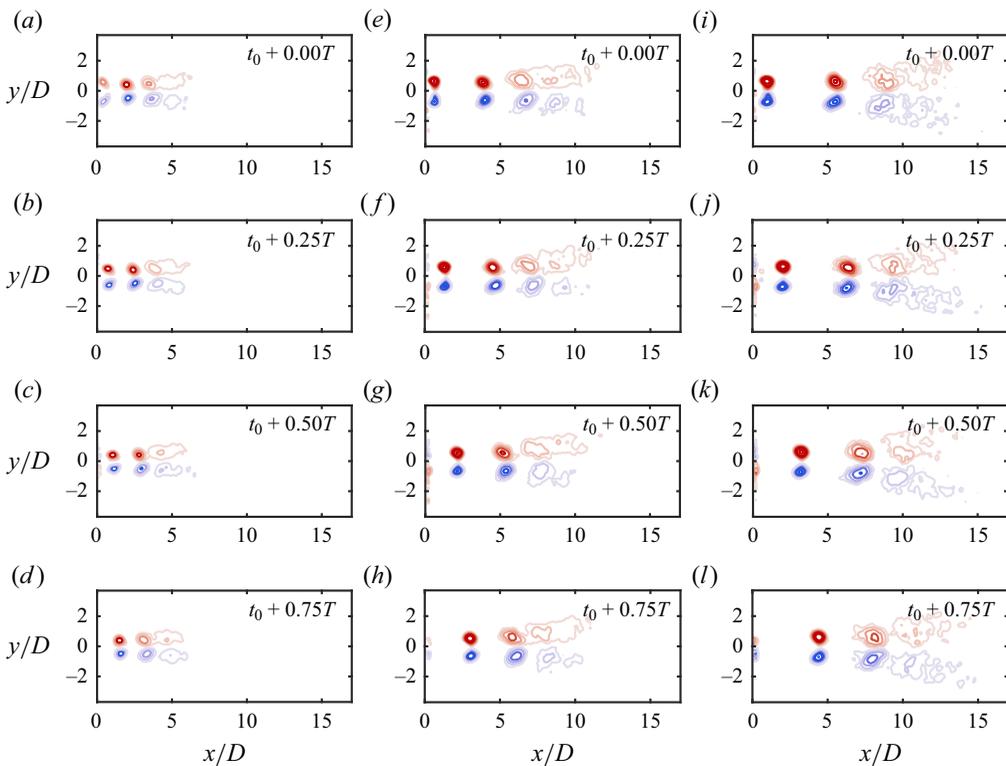


Figure 7. Phase-averaged $\lambda_{ci}D/U_0$ field of the synthetic jet over a period: (*a*–*d*) Case 1; (e-h) Case 2; (*i*–*l*) Case 3. Here $\lambda_{ci}$ is normalised by the orifice diameter $D$ and the time-averaged blowing velocity $U_0$. The sign of $\lambda_{ci}$ is identical to the local vorticity.

rings break down. It can be determined that the synthetic jet vortex rings break down at approximately $x/D = 4.9$, 10.1 and 14.4 for Case 1, Case 2 and Case 3, respectively.

The imaginary part of the complex eigenvalue pair of the velocity gradient tensor, denoted as $\lambda_{ci}$, can be referred to as the local swirling strength of the vortex (Zhou *et al.* 1999), and is used to identify vortices for visually examining the vortex ring breakdown. The phase-averaged $\lambda_{ci}D/U_0$ field is shown in figure 7, with the same contour levels selected in the three cases to plot the vortex evolution. It can be found that the vortex

**980** A5-9

| Term | Equation | Term | Equation |
|------|----------|------|----------|
| Mean volume flux | $Q = 2\displaystyle\int_0^{r_0} \bar{u}r\,\mathrm{d}r$ | Characteristic jet velocity | $u_m = \dfrac{M}{Q}$ |
| Mean momentum flux | $M = 2\displaystyle\int_0^{r_0} \bar{u}^2 r\,\mathrm{d}r$ | Mean turbulence production | $\delta_m = \dfrac{4}{u_m^3 r_m}\displaystyle\int_0^{r_0} \overline{u'v'}\dfrac{\partial \bar{u}}{\partial r} r\,\mathrm{d}r$ |
| Characteristic jet width | $r_m = \dfrac{Q}{M^{1/2}}$ | Mean energy | $\gamma_m = \dfrac{2}{u_m^3 r_m^2}\displaystyle\int_0^{r_0} \bar{u}^3 r\,\mathrm{d}r$ |

Table 2. The terms in (3.10) (Breda & Buxton 2018).

rings maintain a longer streamwise distance as the dimensionless stroke length increases, and their breakdown positions are consistent with those obtained by FMD.

### 3.3. *Entrainment coefficient*

The entrainment coefficient is used to measure the entrainment capacity of jets and plumes, and a detailed description can be found in previous studies (van Reeuwijk & Craske 2015; Breda & Buxton 2018; Xu *et al.* 2023). The entrainment coefficient in a pure jet can be calculated using the following equation:

$$\alpha = -\frac{\delta_m}{2\gamma_m} + \frac{Q}{2M^{1/2}}\frac{\partial}{\partial x}(\ln \gamma_m) = \alpha_1 + \alpha_2. \tag{3.10}$$

The terms in (3.10) are given in table 2. The integral boundary $r_0$ is selected at the radial position of $\bar{u} = 0.02\bar{u}_{cl}$, which is the smallest possible threshold in the present study. A smaller threshold will cause the integral boundary to be outside the FOV or affected by experimental noise at the edge, making it impossible to calculate the entrainment coefficient. It has been checked that the choice of integral boundary $r_0$ from $\bar{u} = 0.02\bar{u}_{cl}$ to $\bar{u} = 0.1\bar{u}_{cl}$ has little effect on the entrainment coefficient, and does not influence the conclusions in this paper. In (3.10), the first term $\alpha_1$ is related to the production of turbulent kinetic energy, and the second term $\alpha_2$ is related to the shape of the velocity profile. According to the velocity triple-decomposition, the Reynolds stress term in $\alpha_1$ can be further decomposed into the coherent Reynolds stress term and the random Reynolds stress term. Correspondingly, $\alpha_1$ is decomposed into $\tilde{\alpha}_1$ and $\hat{\alpha}_1$, representing the contributions of the coherent turbulent kinetic energy production and the random turbulent kinetic energy production to the entrainment coefficient, respectively.

The variations of the entrainment coefficient $\alpha$ and its components for the three cases are shown in figure 8. The entrainment coefficient shows the same trend for all three cases, increasing to a peak value and then decreasing to a constant value in the far field. The entrainment coefficient in the far field is close to the value of 0.057–0.109 found in previous studies for continuous jets (van Reeuwijk & Craske 2015). The entrainment coefficient component $\alpha_2$ is virtually zero, and the components $\tilde{\alpha}_1$ and $\hat{\alpha}_1$ dominate the variation of the entrainment coefficient. Similarly to the variations of the coherent turbulent kinetic energy and random turbulent kinetic energy along the jet centreline, $\tilde{\alpha}_1$ gradually decreases to zero, while $\hat{\alpha}_1$ reaches a peak at the vortex ring breakdown position and completely dominates the entrainment coefficient. Here $\tilde{\alpha}_1$ decreases to zero before the vortex ring breakdown, especially for Case 3, but it is expected that it should decrease to zero at the vortex ring breakdown position. This may be due to the phase identification error caused by the prevalence of multiscale structures in the flow field at large Reynolds
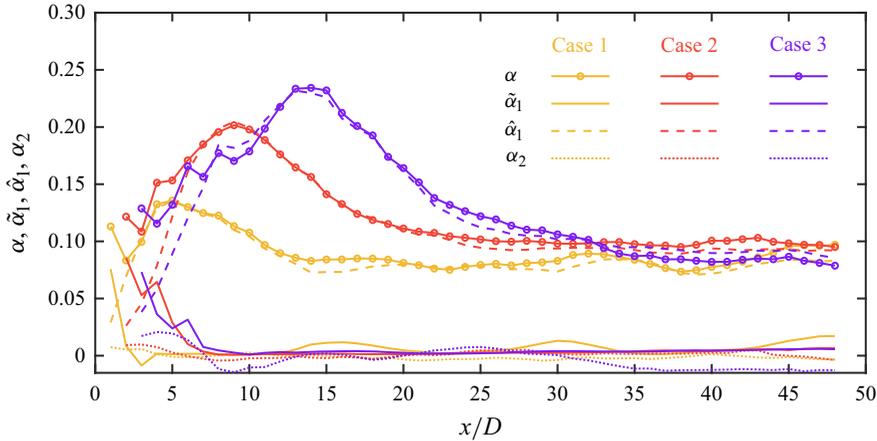
Figure 8. Variations of the entrainment coefficient $\alpha$ and its components for Case 1, Case 2 and Case 3.
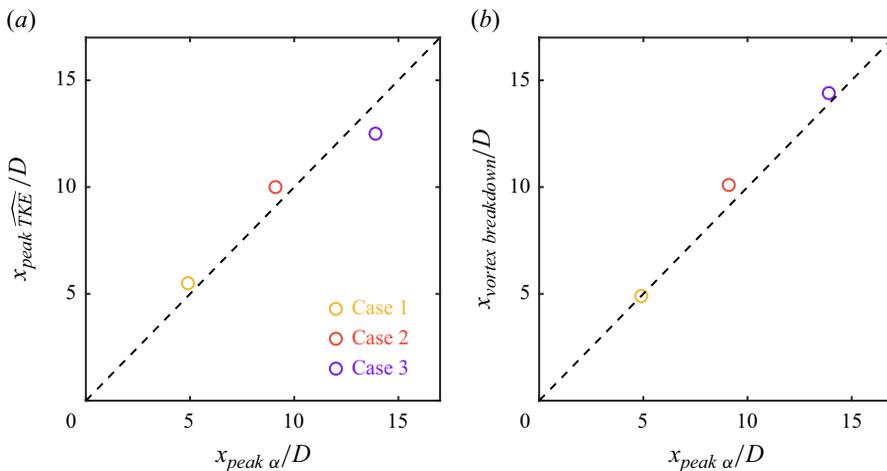


Figure 9. (*a*) Random turbulent kinetic energy peak positions ($x_{peak\widehat{TKE}}$) versus entrainment coefficient peak positions ($x_{peak\ \alpha}$). (*b*) Vortex ring breakdown positions based on the amplitudes of the Fourier mode ($x_{vortex\ breakdown}$) versus entrainment coefficient peak positions ($x_{peak\ \alpha}$). The black dashed line has a slope of 1.

number (Pan *et al.* 2013), which leads to part of the coherent component being classified as the random component. By identifying the maximum points with zero growth rate of entrainment coefficient, the peak positions of entrainment coefficient are determined, which are located at $x/D = 4.9$, 9.1 and 13.9 for Case 1, Case 2 and Case 3, respectively. The peak positions of the entrainment coefficient for the synthetic jets in the three cases are consistent with the vortex ring breakdown positions determined above. It is suggested that the enhanced entrainment of the synthetic jet is due to the increase of the random turbulent kinetic energy term caused by the random small-scale turbulent structure.

### 3.4. *Mechanism of entrainment enhanced by vortex ring breakdown*

The plots of the random turbulent kinetic energy peak positions and the vortex ring breakdown positions versus the entrainment coefficient peak positions are shown in figure 9. As shown in figure 9(*a*), the random turbulent kinetic energy peak positions and
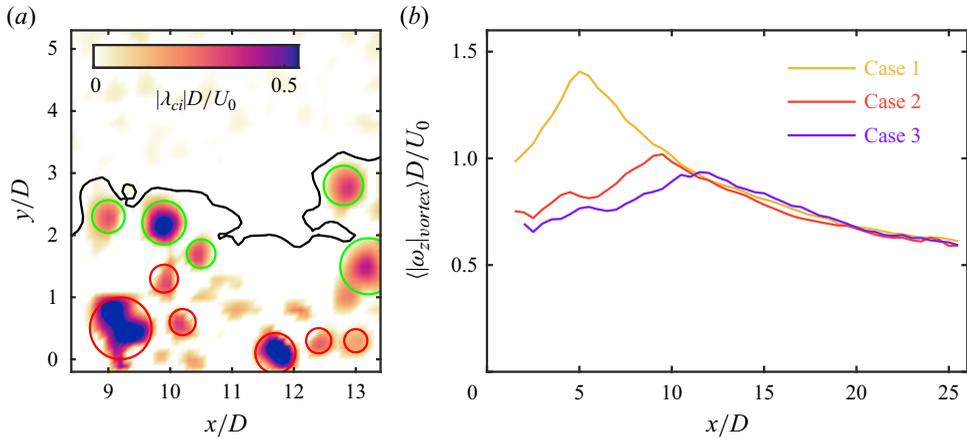
Figure 10. (*a*) Vortices near the TNTI. The black curve represents the irrotational boundary of the TNTI. The green and red circles mark vortices whose centres are less than and greater than $15\eta$ away from the irrotational boundary, respectively. (*b*) Variations of vorticity at the centres of vortices with distance of less than $15\eta$ from the irrotational boundary. The conditional average of the vortices over all snapshots is denoted by $\langle\cdot\rangle$.

the entrainment coefficient peak positions are approximately the same for Case 1 and Case 2. For Case 3, the random turbulent kinetic energy peak position shifts to the upstream, which may be due to the increase of phase identification error at large Reynolds number (Pan *et al.* 2013). As shown in figure 9(*b*), the vortex ring breakdown positions match well the entrainment coefficient peak positions. In addition, it should be emphasised that the effect of the Reynolds number and the dimensionless stroke length on the vortex ring breakdown position can be complex and has not been investigated here. Nevertheless, the above results show the correlation between vortex ring breakdown and enhanced entrainment, and the mechanism of how vortex ring breakdown enhances entrainment will be discussed below.

Figure 10(*a*) shows the vortices near the TNTI and the irrotational boundary of the TNTI in the instantaneous snapshot. The irrotational boundary of the TNTI is detected by the vorticity criterion, whose threshold is determined in the plateau region, where the area of the turbulent region decreases with the threshold with a small slope. It ensures that minor changes in the threshold do not affect the results. A detailed description of this procedure can be found in previous studies (Xu *et al.* 2023). Vortex structures are identified by $\lambda_{ci}$, whose threshold is selected to be 10 % of the maximum $|\lambda_{ci}|$ value in the flow field. It has been checked that varying the threshold from 5 % to 15 % does not affect the results. Figure 10(*b*) shows the variations of vorticity magnitude at the centre of the vortex near the TNTI. Here, only those vortices whose centres are less than $15\eta$ away from the irrotational boundary are included in the statistics, where $\eta$ is the local Kolmogorov scale, and $15\eta$ as the thickness of TNTI has been confirmed by previous studies (Zecchetto & da Silva 2021; Xu *et al.* 2023). The vorticity magnitude at the centre of the vortex near the TNTI reaches peak value at $x/D = 5.1$, 9.3 and 11.7 for Case 1, Case 2 and Case 3, respectively, which corresponds to the vortex ring breakdown position. The vortex ring breakdown results in the transfer of turbulent kinetic energy from the coherent large-scale structure to the random small-scale structure, enhancing the vortices near the TNTI. The vortex near the TNTI will induce a counterflow velocity field which implies that fluid from both sides of the TNTI is transported towards the TNTI, resulting in a compressive strain normal to the TNTI and an extensive strain parallel to the TNTI (Watanabe *et al.* 2014; Mistry *et al.* 2019). The alignment of the extensive strain and the vorticity vector

**980** A5-12

results in a larger enstrophy production, allowing more environment irrotational fluid to gain vorticity, thereby enhancing local entrainment.

## 4. Conclusion

In the present study, the synthetic jets with different Reynolds numbers and dimensionless stroke lengths are measured using the TR-2DPIV technique. The results of velocity triple-decomposition show that the coherent turbulent kinetic energy gradually decreases to zero, while the random turbulent kinetic energy reaches a peak value when the vortex ring breaks down and then decreases to a constant value in the far field, indicating that a transition of turbulent kinetic energy from large-scale to small-scale. The global power spectrum shows that the near field of the synthetic jet is dominated by the vortex ring generated by the actuator. The high-amplitude region in the Fourier mode at the characteristic frequency of $f/f_d = 1$ highlights the region dominated by the vortex ring. According to the streamwise position where the high-amplitude region disappears, it can be determined that the synthetic jet vortex ring breaks down at approximately $x/D = 4.9$, 10.1 and 14.4 for the three cases, respectively. In addition, the process of vortex ring breakdown is visually examined by the phase-averaged $\lambda_{ci}D/U_0$ field. The entrainment coefficient $\alpha$, which measures the entrainment capacity of jets, is decomposed into three components: $\tilde{\alpha}_1$; $\hat{\alpha}_1$; $\alpha_2$. These components represent the contribution of the coherent turbulent kinetic energy production term, the random turbulent kinetic energy production term and the shape of the velocity profile to the entrainment coefficient, respectively. The contribution of component $\alpha_2$ is almost negligible. Here $\tilde{\alpha}_1$ decreases to zero as the flow develops, while $\hat{\alpha}_1$ reaches a peak value at the vortex ring breakdown position and completely dominates the entrainment coefficient. The entrainment coefficient peak positions for the three cases are consistent with the vortex ring breakdown positions determined above. Based on the analysis of the vortices near the TNTI, it is found that the strength of the vortex near the TNTI is enhanced by the vortex ring breakdown, which will lead to the enhancement of the enstrophy production, and thus increase local entrainment.

**Declaration of interests.** The authors report no conflict of interest.

**Author ORCIDs.**

Congyi Xu https://orcid.org/0000-0003-1093-7561;

Jinjun Wang https://orcid.org/0000-0001-9523-7403.

REFERENCES

BALAMURUGAN, G., RODDA, A., PHILIP, J. & MANDAL, A.C. 2020 Characteristics of the turbulent non-turbulent interface in a spatially evolving turbulent mixing layer. *J. Fluid Mech.* **894**, A4.

BORRELL, G. & JIMENEZ, J. 2016 Properties of the turbulent/non-turbulent interface in boundary layers. *J. Fluid Mech.* **801**, 554–596.

BREDA, M. & BUXTON, O.R.H. 2018 Influence of coherent structures on the evolution of an axisymmetric turbulent jet. *Phys. Fluids* **30** (3), 035109.

BREDA, M. & BUXTON, O.R.H. 2019 Behaviour of small-scale turbulence in the turbulent/non-turbulent interface region of developing turbulent jets. *J. Fluid Mech.* **879**, 187–216.

CATER, J.E. & SORIA, J. 2002 The evolution of round zero-net-mass-flux jets. *J. Fluid Mech.* **472**, 167–200.

CHAMPAGNAT, F., PLYER, A., LE BESNERAIS, G., LECLAIRE, B., DAVOUST, S. & LE SANT, Y. 2011 Fast and accurate PIV computation using highly parallel iterative correlation maximization. *Exp. Fluids* **50** (4), 1169–1182.

CHAUHAN, K., PHILIP, J., DE SILVA, C.M., HUTCHINS, N. & MARUSIC, I. 2014 The turbulent/non-turbulent interface and entrainment in a boundary layer. *J. Fluid Mech.* **742**, 119–151.

CHEN, J.G. & BUXTON, O.R.H. 2023 Spatial evolution of the turbulent/turbulent interface geometry in a cylinder wake. *J. Fluid Mech.* **969**, A4.

FENG, L.H. & WANG, J.J. 2010 Circular cylinder vortex-synchronization control with a synthetic jet positioned at the rear stagnation point. *J. Fluid Mech.* **662**, 232–259.

FENG, L.H. & WANG, J.J. 2012 Synthetic jet control of separation in the flow over a circular cylinder. *Exp. Fluids* **53** (2), 467–480.

HOLMAN, R., UTTURKAR, Y., MITTAL, R., SMITH, B.L. & CATTAFESTA, L. 2005 Formation criterion for synthetic jets. *AIAA J.* **43** (10), 2110–2116.

JAHANBAKHSHI, R. & MADNIA, C.K. 2016 Entrainment in a compressible turbulent shear layer. *J. Fluid Mech.* **797**, 564–603.

JAHANBAKHSHI, R. & MADNIA, C.K. 2018 The effect of heat release on the entrainment in a turbulent mixing layer. *J. Fluid Mech.* **844**, 92–126.

JAMES, R.D., JACOBS, J.W. & GLEZER, A. 1996 A round turbulent jet produced by an oscillating diaphragm. *Phys. Fluids* **8** (9), 2484–2495.

KANKANWADI, K.S. & BUXTON, O.R.H. 2020 Turbulent entrainment into a cylinder wake from a turbulent background. *J. Fluid Mech.* **905**, A35.

KANKANWADI, K.S. & BUXTON, O.R.H. 2022 On the physical nature of the turbulent/turbulent interface. *J. Fluid Mech.* **942**, A31.

KRISHAN, G., AW, K.C. & SHARMA, R.N. 2019 Synthetic jet impingement heat transfer enhancement – a review. *Appl. Therm. Engng* **149**, 1305–1323.

KRISHNAN, G. & MOHSENI, K. 2009 Axisymmetric synthetic jets: an experimental and theoretical examination. *AIAA J.* **47** (10), 2273–2283.

LI, S.C., LONG, Y.G. & WANG, J.J. 2022 Turbulent/non-turbulent interface for laminar boundary flow over a wall-mounted fence. *Phys. Fluids* **34** (12), 125113.

LONG, Y.G., WANG, J.J. & PAN, C. 2022 Universal modulations of large-scale motions on entrainment of turbulent boundary layers. *J. Fluid Mech.* **941**, A68.

MA, L.Q., FENG, L.H., PAN, C., GAO, Q. & WANG, J.J. 2015 Fourier mode decomposition of PIV data. *Sci. China Technol. Sci.* **58** (11), 1935–1948.

MALLINSON, S.G., REIZES, J.A. & HONG, G. 2001 An experimental and numerical study of synthetic jet flow. *Aeronaut. J.* **105** (1043), 41–49.

MATHEW, J. & BASU, A.J. 2002 Some characteristics of entrainment at a cylindrical turbulence boundary. *Phys. Fluids* **14** (7), 2065–2072.

MISTRY, D., PHILIP, J. & DAWSON, J.R. 2019 Kinematics of local entrainment and detrainment in a turbulent jet. *J. Fluid Mech.* **871**, 896–924.

MISTRY, D., PHILIP, J., DAWSON, J.R. & MARUSIC, I. 2016 Entrainment at multi-scales across the turbulent/non-turbulent interface in an axisymmetric jet. *J. Fluid Mech.* **802**, 690–725.

NEAMTU-HALIC, M.M., KRUG, D., MOLLICONE, J.-P., VAN REEUWIJK, M., HALLER, G. & HOLZNER, M. 2020 Connecting the time evolution of the turbulence interface to coherent structures. *J. Fluid Mech.* **898**, A3.

PAN, C., WANG, H.P. & WANG, J.J. 2013 Phase identification of quasi-periodic flow measured by particle image velocimetry with a low sampling rate. *Meas. Sci. Technol.* **24** (5), 055305.

PAN, C., XUE, D., XU, Y., WANG, J.J. & WEI, R.J. 2015 Evaluating the accuracy performance of Lucas–Kanade algorithm in the circumstance of PIV application. *Sci. China Phys. Mech. Astron.* **58** (10), 104704.

VAN REEUWIJK, M. & CRASKE, J. 2015 Energy-consistent entrainment relations for jets and plumes. *J. Fluid Mech.* **782**, 333–355.

REYNOLDS, W.C. & HUSSAIN, A.K.M.F. 1972 The mechanics of an organized wave in turbulent shear flow. Part 3. Theoretical models and comparisons with experiments. *J. Fluid Mech.* **54** (2), 263–288.

SHUSTER, J.M. & SMITH, D.R. 2007 Experimental study of the formation and scaling of a round synthetic jet. *Phys. Fluids* **19** (4), 045109.

DA SILVA, C.B., HUNT, J.C.R., EAMES, I. & WESTERWEEL, J. 2014 Interfacial layers between regions of different turbulence intensity. *Annu. Rev. Fluid Mech.* **46** (1), 567–590.

SMITH, B.L. & GLEZER, A. 1998 The formation and evolution of synthetic jets. *Phys. Fluids* **10** (9), 2281–2297.

SMITH, B.L. & SWIFT, G.W. 2003 A comparison between synthetic jets and continuous jets. *Exp. Fluids* **34** (4), 467–472.

TAVEIRA, R.R., DIOGO, J.S., LOPES, D.C. & DA SILVA, C.B. 2013 Lagrangian statistics across the turbulent-nonturbulent interface in a turbulent plane jet. *Phys. Rev.* E **88** (4), 043001.

WATANABE, T., SAKAI, Y., NAGATA, K., ITO, Y. & HAYASE, T. 2014 Vortex stretching and compression near the turbulent/non-turbulent interface in a planar jet. *J. Fluid Mech.* **758**, 754–785.

WESTERWEEL, J., FUKUSHIMA, C., PEDERSEN, J.M. & HUNT, J.C.R. 2005 Mechanics of the turbulent-nonturbulent interface of a jet. *Phys. Rev. Lett.* **95** (17), 174501.

WESTERWEEL, J., FUKUSHIMA, C., PEDERSEN, J.M. & HUNT, J.C.R. 2009 Momentum and scalar transport at the turbulent/non-turbulent interface of a jet. *J. Fluid Mech.* **631**, 199–230.

XIA, X. & MOHSENI, K. 2018 Transitional region of a round synthetic jet. *Phys. Rev. Fluids* **3** (1), 011901.

XU, C.Y., LONG, Y.G. & WANG, J.J. 2023 Entrainment mechanism of turbulent synthetic jet flow. *J. Fluid Mech.* **958**, A31.

XU, Y., MOON, C., WANG, J.J., PENYAZKOV, O.G. & KIM, K.C. 2019 An experimental study on the flow and heat transfer of an impinging synthetic jet. *Intl J. Heat Mass Transfer* **144**, 118626.

ZECCHETTO, M. & DA SILVA, C.B. 2021 Universality of small-scale motions within the turbulent/non-turbulent interface layer. *J. Fluid Mech.* **916**, A9.

ZHANG, B.L., LIU, H., LI, Y.Y., LIU, H. & DONG, J.Z. 2021*a* Experimental study of coaxial jets mixing enhancement using synthetic jets. *Appl. Sci. Basel* **11** (2), 803.

ZHANG, H.Y., RIVAL, D.E. & WU, X.H. 2021*b* Kinematics of the turbulent and nonturbulent interfaces in a subsonic airfoil flow. *AIAA J.* **59** (6), 2155–2168.

ZHANG, X.X., WATANABE, T. & NAGATA, K. 2023 Reynolds number dependence of the turbulent/non-turbulent interface in temporally developing turbulent boundary layers. *J. Fluid Mech.* **964**, A8.

ZHOU, J., ADRIAN, R.J., BALACHANDAR, S. & KENDALL, T.M. 1999 Mechanisms for generating coherent packets of hairpin vortices in channel flow. *J. Fluid Mech.* **387**, 353–396.

ZONG, H.H., VAN PELT, T. & KOTSONIS, M. 2018 Airfoil flow separation control with plasma synthetic jets at moderate Reynolds number. *Exp. Fluids* **59** (11), 169.